Hysteretic Flux Response and Nondegenerate Gain of Flux-Driven Josephson Parametric Amplifiers

Stefan Pogorzalek, Kirill G. Fedorov, Ling Zhong, Jan Goetz, Friedrich Wulschner, Michael Fischer, Peter Eder, Edwar Xie, Kunihiro Inomata, Tsuyoshi Yamamoto, Yasunobu Nakamura, Achim Marx, Frank Deppe, and Rudolf Gross

Phys. Rev. Applied **8**, 024012 — Published 17 August 2017

DOI: 10.1103/PhysRevApplied.8.024012

Hysteretic flux response and nondegenerate gain of flux-driven Josephson parametric amplifiers

Stefan Pogorzalek,[1,2,*] Kirill G. Fedorov,[1,2] Ling Zhong,[1,2,3] Jan Goetz,[1,2] Friedrich Wulschner,[1,2] Michael Fischer,[1,2,3] Peter Eder,[1,2,3] Edwar Xie,[1,2,3] Kunihiro Inomata,[4] Tsuyoshi Yamamoto,[4,5] Yasunobu Nakamura,[6] Achim Marx,[1] Frank Deppe,[1,2,3] and Rudolf Gross[1,2,3,†]

[1] *Walther-Meißner-Institut, Bayerische Akademie der Wissenschaften, 85748 Garching, Germany*
[2] *Physik-Department, Technische Universität München, 85748 Garching, Germany*
[3] *Nanosystems Initiative Munich (NIM), Schellingstraße 4, 80799 München, Germany*
[4] *RIKEN Center for Emergent Matter Science (CEMS), Wako, Saitama 351-0198, Japan*
[5] *NEC IoT Devices Research Laboratories, Tsukuba, Ibaraki 305-8501, Japan*
[6] *Research Center for Advanced Science and Technology (RCAST), The University of Tokyo, Meguro-ku, Tokyo 153-8904, Japan*

(Dated: July 16, 2017)

Josephson parametric amplifiers (JPA) have become key devices in quantum science and technology with superconducting circuits. In particular, they can be utilized as quantum-limited amplifiers or as a source of squeezed microwave fields. Here, we report on the detailed measurements of five flux-driven JPAs exhibiting a hysteretic dependence of the resonant frequency on the applied magnetic flux. We model the measured characteristics by numerical simulations based on the two-dimensional potential landscape of the dc superconducting quantum interference devices (dc-SQUID), which provide the JPA nonlinearity, for a non-zero screening parameter $\beta_L > 0$ and demonstrate excellent agreement between the numerical results and the experimental data. Furthermore, we study the nondegenerate response of different JPAs and accurately describe the experimental results with our theory.

PACS numbers: 85.25.Cp, 85.25.Dq, 85.25.-j
Keywords: Josephson parametric amplifier, Josephson junctions, dc-SQUID

I. INTRODUCTION

The field of superconducting quantum circuits (SQC) is a highly active field of research with outstanding progress over the last decade. Typically, the circuits are operated at microwave frequencies and therefore profit from commercially available low-noise amplifiers. However, the operation of SQCs often requires quantum-limited amplification of weak signals over a broad frequency range. For this purpose, one can either use broadband traveling wave parametric amplifiers [1, 2] or band tunable narrow-band JPAs [3–6]. The latter are nowadays routinely used to provide amplification with a noise performance close to the standard quantum limit [7–12]. Moreover, if operated in the phase sensitive regime, JPAs can even achieve noise temperatures below the standard quantum limit [11, 13, 14]. JPAs also have been shown to generate squeezed microwave light [15–20], which can be be utilized in numerous quantum information processing algorithms. A particularly prominent application is the generation of entanglement in the form of two-mode squeezed propagating microwave states [20–22] as required for many quantum communication and quantum teleportation protocols with continuous variables [23]. Also, the bipartite entanglement of the emitted light modes allows one to detect low reflectivity objects in quantum illumination protocols more efficiently than in the classical case [24, 25]. Furthermore, squeezed states are of importance in the context of quantum computing with continuous variables [21, 26, 27].

The fundamental understanding and quantitative description of different operation regimes of JPAs are crucial for their optimization and adaptation for specific applications. In this context, we study JPAs consisting of a superconducting coplanar waveguide resonator short-circuited to ground by a dc-SQUID. In particular, we investigate how the resonant frequency of five JPAs with different screening parameters of the constituent dc-SQUID depends on the magnetic flux threading the dc-SQUID loop. From numerical simulations of the dc-SQUID potential, we find that the flux dependence of the JPA resonant frequency is, in general, hysteretic for arbitrary screening parameters of the dc-SQUID and find good agreement with experimental observations. Furthermore, we report on the nondegenerate gain properties when applying a pump tone to the JPAs. The JPA response depends strongly on the resonator characteristics and coincides accurately with our theoretical predictions for a flux-driven JPA.

The rest of this paper is structured as follows. An introduction of the flux-driven JPA in Sec. II is followed by a theoretical description of the dependence of the JPA resonant frequency on an external flux in Sec. III. The behavior of the dc-SQUID potential as a function of the external flux is described in Sec. IV. In Sec. V, we present the experimentally measured flux dependence of the JPA

* stefan.pogorzalek@wmi.badw.de
† rudolf.gross@wmi.badw.de

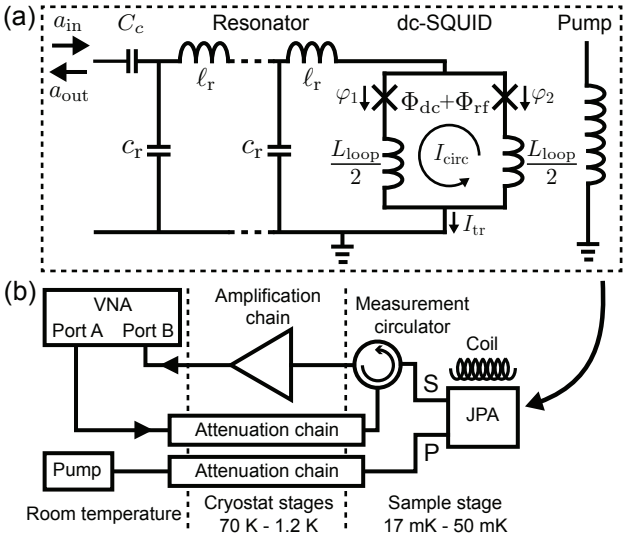

Figure 1. (a) Circuit diagram of a JPA consisting of a coplanar waveguide resonator with inductance $\ell_{\rm r}$ and capacitance $c_{\rm r}$ per unit length which add up to the total inductance $L_{\rm r}$ and capacitance $C_{\rm r}$. The dc-SQUID loop has a non-zero loop inductance $L_{\rm loop}$ and, thus, inductively couples to a magnetic flux $\Phi_{\rm dc}+\Phi_{\rm rf}$ generated by a coil and a pump line, respectively. Crosses indicate Josephson junctions. (b) Setup for the characterization of JPAs with a VNA. The reflected signal from the JPA is separated from the input signal by a measurement circulator. The current through a superconducting coil determines the flux $\Phi_{\rm dc}$ through the dc-SQUID loop. S and P mark the signal and pump port, respectively.

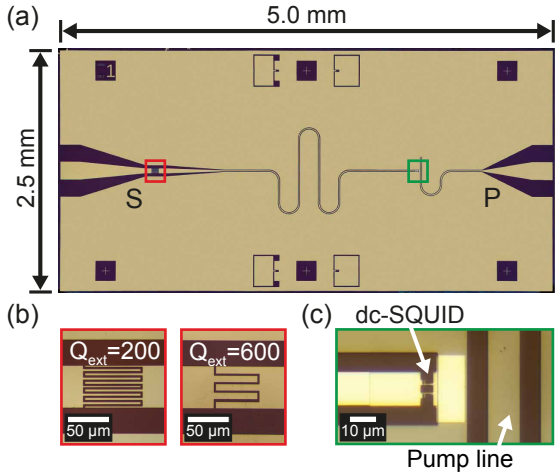

Figure 2. (a) Optical micrograph of a JPA sample chip. Red and green rectangles mark the coupling capacitor and the dc-SQUID with the pump line, respectively. S and P mark the signal and pump ports, respectively. (b) Zoom-ins to coupling capacitors with a designed external quality factor of $Q_{\rm ext}=200$ (left), $Q_{\rm ext}=600$ (right). (c) Zoom-in to the dc-SQUID with the adjacent pump line. The size of the dc-SQUID loop is $3.4\times2.4\,\mu{\rm m}^2$.

resonant frequency and compare it to theory. Finally, we investigate the nondegenerate gain properties for two JPAs with different parameters in Sec. VI and summarize our results in Sec. VII.

II. THE FLUX-DRIVEN JPA

We investigate a flux-driven JPA [3] consisting of a quarter-wavelength coplanar waveguide resonator which is short-circuited to ground by a dc-SQUID [see Fig. 1(a)]. The dc-SQUID provides a flux-tunable nonlinear inductance which contributes to the quasi-static resonant frequency ω_0 of the JPA. Thus, a magnetic flux can be used to tune the dc-SQUID inductance and, in this way, the resonant frequency of the whole circuit. An on-chip antenna couples inductively to the dc-SQUID loop with an inductance $L_{\rm loop}$ and is used to apply a strong coherent pump tone with a frequency $\omega_{\rm pump}=2\omega_0$. The pump tone leads to a periodic modulation of the dc-SQUID inductance and, thus, to a periodic variation of the resonant frequency of the JPA around ω_0 which gives rise to parametric effects [28, 29]. A signal mode with frequency $\omega_{\rm s}=\omega_{\rm pump}/2+\delta\omega$ incident to the JPA input port is then amplified, while at the same time an idler mode at frequency $\omega_{\rm i}=\omega_{\rm pump}/2-\delta\omega$ is generated so that the total energy is conserved, $\omega_{\rm pump}=\omega_{\rm s}+\omega_{\rm i}$ [30].

In order to experimentally characterize the JPAs, we use the setup shown in Fig. 1(b). A vector network analyzer (VNA) applies a probe signal to the JPA via a measurement circulator, which separates the incoming signal from the signal reflected at the JPA. Subsequently, the reflected signal is amplified with cryogenic and room temperature amplifiers, and measured by the VNA to obtain the complex reflection coefficient S_{11}. The external magnetic field is generated by a superconducting coil. For nondegenerate gain measurements, a strong coherent pump tone is applied in addition to the VNA probe tone.

The JPA sample is encased inside a gold-plated copper box and mounted to the base temperature stage of a dilution refrigerator. In Fig. 2, we show an optical micrograph of a JPA sample and magnified views of the coupling capacitor and the dc-SQUID region. All presented samples were fabricated at NEC and RIKEN, Japan. Resonator and pump line consist of a 50 nm thick niobium film which is sputter-deposited onto a 300 μm thick thermally oxidized silicon substrate. Both resonator and pump line have a coplanar waveguide geometry with an impedance of 50 Ω. The dc-SQUID is fabricated with aluminum technology and double angle shadow evaporation [31].

III. THEORY OF THE RESONANT FREQUENCY OF A TUNABLE JPA

In this section, we describe how the resonant frequency of the JPA circuit depends on an external magnetic flux $\Phi_{\rm ext}$ threading the dc-SQUID loop. The treatment is

applicable for arbitrary flux-screening of the dc-SQUID, which can be quantified by the dimensionless screening parameter β_L defined below. Based on a distributed element model for a quarter-wavelength resonator and a lumped element model for the dc-SQUID [see Fig. 1(a)], one arrives at a transcendental equation for the resonant frequency ω_0 of the JPA [32, 33]

$$\frac{\pi\omega_0}{2\omega_\mathrm{r}}\tan\left(\frac{\pi\omega_0}{2\omega_\mathrm{r}}\right)=\frac{(2\pi)^2}{\Phi_0^2}L_\mathrm{r}E_s(\Phi_\mathrm{ext})-\frac{2C_\mathrm{s}}{C_\mathrm{r}}\left(\frac{\pi\omega_0}{2\omega_\mathrm{r}}\right)^2. \quad (1)$$

Here, L_r, C_r, and $\omega_\mathrm{r}=1/\sqrt{L_\mathrm{r}C_\mathrm{r}}$ are the total inductance, the total capacitance and the resonant frequency of the bare resonator, respectively, $E_\mathrm{s}(\Phi_\mathrm{ext})$ is the flux-dependent energy of the dc-SQUID defined below, and C_s is the capacitance of one Josephson junction. For the investigated samples, the last term in Eq. (1) can be neglected, since the capacitance of the resonator strongly exceeds the one of the Josephson junctions, $C_\mathrm{r}\gg C_\mathrm{s}$. For a vanishing transport current I_tr through the dc-SQUID, we define the Josephson inductance of the dc-SQUID as

$$L_\mathrm{s}(\Phi_\mathrm{ext})=\frac{\Phi_0}{4\pi I_\mathrm{c}|\cos\varphi_-^\mathrm{min}(\Phi_\mathrm{ext})|}, \quad (2)$$

where I_c is the critical current of a single Josephson junction and $\varphi_\pm\equiv(\varphi_1\pm\varphi_2)/2$ is derived from the phase differences φ_1 and φ_2 across each of the Josephson junctions of the dc-SQUID. Here, $\varphi_\pm^\mathrm{min}(\Phi_\mathrm{ext})$ are the steady-state phase differences for a given external flux Φ_ext. Then, one can express the flux-dependent energy of the dc-SQUID as

$$E_\mathrm{s}(\Phi_\mathrm{ext})=\frac{\Phi_0^2}{(2\pi)^2}\frac{1}{L_\mathrm{s}(\Phi_\mathrm{ext})+L_\mathrm{loop}/4}, \quad (3)$$

where also the non-zero dc-SQUID loop inductance L_loop is taken into account [34].

For $\omega_0/\omega_\mathrm{r}\simeq 1$, the tangent in Eq. (1) can be expanded near $\pi/2$ with a Laurent expansion to obtain a simplified expression for the resonant frequency of the JPA in terms of inductances

$$\omega_0(\Phi_\mathrm{ext})=\omega_\mathrm{r}\left[1+\frac{L_\mathrm{s}(\Phi_\mathrm{ext})+L_\mathrm{loop}/4}{L_\mathrm{r}}\right]^{-1}. \quad (4)$$

We now discuss the effect of flux-screening of the dc-SQUID. In general, $\varphi_-^\mathrm{min}(\Phi_\mathrm{ext})$ exhibits a non-trivial dependence on the external magnetic flux. Due to the fluxoid quantization, $\varphi_-^\mathrm{min}(\Phi_\mathrm{ext})$ is related to the total flux $\Phi=\Phi_\mathrm{ext}+L_\mathrm{loop}I_\mathrm{circ}$ threading the dc-SQUID as $\varphi_-^\mathrm{min}=\pi(\Phi/\Phi_0)$. The total flux is given by the sum of the external flux Φ_ext and a part $\Phi_\mathrm{circ}=L_\mathrm{loop}I_\mathrm{circ}$ originating from the supercurrent I_circ circulating in the dc-SQUID loop. To account for this screening current, we introduce the dimensionless screening parameter [35]

$$\beta_\mathrm{L}\equiv\frac{2L_\mathrm{loop}I_\mathrm{c}}{\Phi_0}. \quad (5)$$

In the case of a vanishing screening parameter $\beta_\mathrm{L}\simeq 0$, we have $\Phi\approx\Phi_\mathrm{ext}$. In this case, the fluxoid quantization fixes the phase of one Josephson junction relative to the other one, reducing the available degrees of freedom from two to one. This results in a single-valued dependence $\varphi_-^\mathrm{min}=\pi(\Phi_\mathrm{ext}/\Phi_0)$ and one obtains the well-known expression for the flux-dependent inductance of a dc-SQUID, $L_\mathrm{s}(\Phi_\mathrm{ext})=\Phi_0/(4\pi I_\mathrm{c}|\cos\pi(\Phi_\mathrm{ext}/\Phi_0)|)$ [36]. A mechanical analog of this situation are two rigidly coupled pendula, where the system can be described by a single deflection angle, i.e., a single degree of freedom due to the rigid coupling. However, if the screening parameter β_L becomes non-zero, there is no analytic expression for $\varphi_-^\mathrm{min}(\Phi_\mathrm{ext})$ anymore and the dependence has to be calculated numerically.

IV. SIMULATION OF THE DC-SQUID POTENTIAL

We now discuss hysteretic dc-SQUIDs for non-zero screening $\beta_\mathrm{L}>0$. To illustrate the behavior of a dc-SQUID in equilibrium, we consider a phase particle in the dc-SQUID potential [37]

$$\frac{U(\varphi_+,\varphi_-)}{E_\mathrm{J}}=2-2\cos\varphi_+\cos\varphi_-+2j_\mathrm{tr}\varphi_+ +\frac{2}{\pi\beta_\mathrm{L}}\left(\varphi_--\pi\frac{\Phi_\mathrm{ext}}{\Phi_0}\right)^2, \quad (6)$$

where $j_\mathrm{tr}\equiv I_\mathrm{tr}/2I_\mathrm{c}$ is the normalized transport current through the dc-SQUID and $E_\mathrm{J}\equiv I_\mathrm{c}\Phi_0/2\pi$ is the coupling energy of a single Josephson junction. Figure 3 shows the potential $U(\varphi_+,\varphi_-)$ calculated according to Eq. (6) for different values of the external flux Φ_ext and with a typical experimental value of $\beta_\mathrm{L}=0.6$ as well as $j_\mathrm{tr}=0$. Note that for $j_\mathrm{tr}=0$ there is no tilt of the potential landscape along the φ_+-direction. In contrast to other works investigating hysteretic dc-SQUIDs [37–39], in our experiments the transport current j_tr is negligible at all times, meaning that the possible equilibrium phase differences $(\varphi_+^\mathrm{min},\varphi_-^\mathrm{min})$ of the dc-SQUID are given by the local minima shown in Fig. 3. One can consider a phase particle with coordinates $(\varphi_+^\mathrm{min},\varphi_-^\mathrm{min})$ residing in one of the minima. Due to the periodicity of the potential, multiple equivalent local minima, which describe the same state of the dc-SQUID, exist. For $\Phi_\mathrm{ext}=0$, all local minima are degenerate. However, for non-zero Φ_ext and β_L there are two classes of minima corresponding to clock- and counter-clock-wise circulating screening currents. One is shifted upwards and the other one downwards in energy, therefore corresponding to a class of metastable and stable states, respectively.

In order to obtain $\varphi_-^\mathrm{min}(\Phi_\mathrm{ext})$, one can track the equilibrium positions of the phase particle for a continuously varied external magnetic flux. Figure 3 illustrates the behavior of the phase particle (shown as a white dot) for increasing and decreasing external flux. In the following,

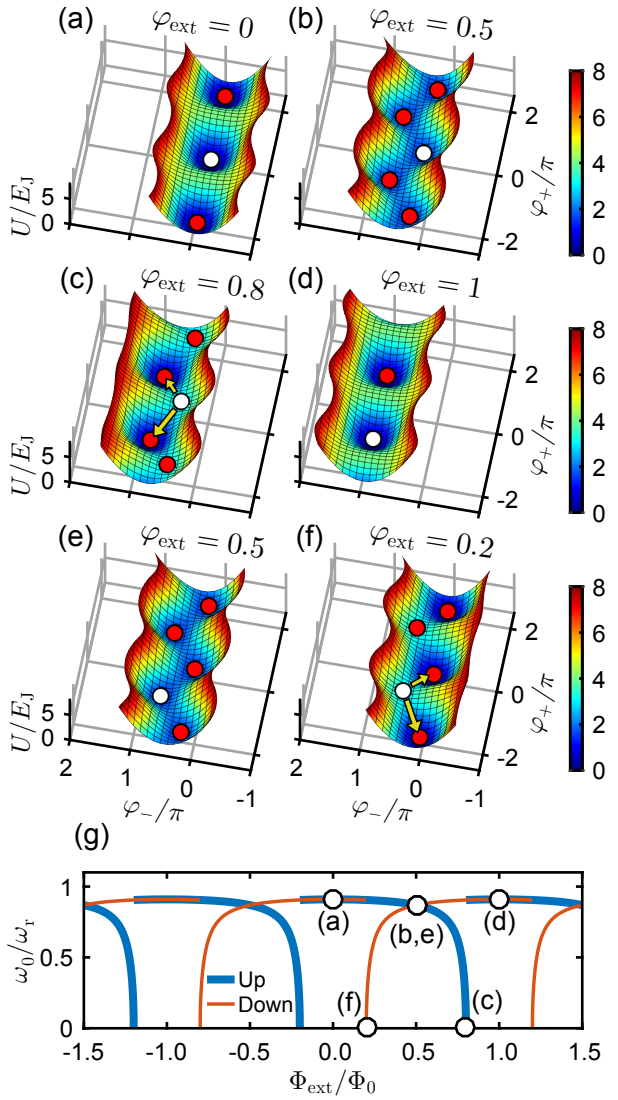

Figure 3. (a-f) Two-dimensional dc-SQUID potential U for different external flux values Φ_{ext} with $\beta_L = 0.6$ and $j_{tr} = 0$. White dots denote the present position of the phase particle, whereas red dots indicate the positions of all other local minima. Panels (a-d) and panels (e,f) correspond to increasing and decreasing Φ_{ext}, respectively. Arrows indicate a jump of the phase particle to an adjacent minimum, when the present local minimum disappears. (g) JPA resonant frequency ω_0 when sweeping Φ_{ext} towards larger (blue) and smaller (orange) values, calculated from Eq. (1) with $L_{loop} = 0$, $L_r = 10 L_{s,min}$ and $L_{s,min} = \Phi_0/(4\pi I_c)$. Furthermore, the ω_0 values of the corresponding position of the phase particle in panels (a-f) are denoted by white dots in panel (g).

we neglect thermally activated and tunneling processes. That is, we assume that the phase particle resides in one specific minimum as long as this minimum exists. If the external flux Φ_{ext} and therefore φ_-^{min} is changed such that this minimum vanishes, the phase particle will move to one of the two adjacent minima. Because the adjacent minima always belong to a different class of local minima, one obtains a discontinuity in $\varphi_-^{min}(\Phi_{ext})$. The position of this discontinuity depends on the magnitude of β_L. This discontinuity, in turn, leads to a discontinuity of the dc-SQUID inductance $L_s(\Phi_{ext})$, which can be experimentally observed as a jump of the JPA resonant frequency $\omega_0(\Phi_{ext})$. Evaluating Eq. (4) with the obtained $\varphi_-^{min}(\Phi_{ext})$ can then be used to derive the flux dependence of the resonant frequency for the whole JPA circuit.

In addition, from the simulations we expect that there is always a hysteretic behavior for non-zero β_L. However, for small β_L, hysteresis only appears at frequencies much smaller than the maximum resonant frequency. Furthermore, a very small hysteresis may also be smeared out by thermally activated hopping between adjacent local energy minima in the experiments. Nevertheless, the behavior observed in our devices is markedly different from the textbook discussion of the total flux in a dc-SQUID as a function of the external flux. There, the hysteretic behavior only occurs above a certain threshold value $\beta_L \geq 2/\pi$ of the screening parameter [35], whereas, in our devices, hysteretic behavior is already observed for $\beta_L \ll 2/\pi$. The reason for this difference is that we take into account the full dc-SQUID potential without any simplifications.

The two-dimensional potential landscapes shown in Fig. 3 have been calculated for $j_{tr} = 0$. However, in our experiments shown below, a finite microwave signal is applied resulting in a finite microwave current across the dc-SQUID which resides in a current anti-node of the resonator. This finite microwave current results in a periodic tilt of the dc-SQUID potential along the φ_+-axis. Of course, this periodic tilt affects the dynamics of the phase particle. However, in our experiments the applied microwave signal is very small, resulting in microwave currents which are at least two orders of magnitude smaller than the junction critical current. As a consequence, the tiny periodic tilt of the dc-SQUID potential along the φ_+-axis can be neglected when analyzing the phase dynamics. Note that the finite microwave current results in a smearing of the hysteretic φ_-^{min} versus Φ_{ext} dependence similar to thermal or other noise currents.

V. EXPERIMENTAL MEASUREMENTS OF THE JPA FLUX DEPENDENCE

In order to experimentally investigate the properties of hysteretic JPAs, we study five samples (JPA 1 to JPA 5) with different screening parameters as well as different external and internal quality factors. While JPA 1 and JPA 2 have small screening parameters and high internal quality factors, JPA 3 to JPA 5 have larger screening parameters of $\beta_L \simeq 0.5$ and lower internal quality factors (see Tab. I). The larger β_L values for samples JPA 3 to JPA 5 are explained by higher critical currents I_c of the Josephson junctions. In the experiments discussed in this section, no additional external pump signal is applied to the JPA.

Table I. Parameters extracted from fitting of the flux-dependent JPA resonant frequency for different samples with the estimation of $L_r = 2\,\mathrm{nH}$. External quality factors Q_{ext} and internal quality factors Q_{int} are obtained from fits using Eq. (7).

Sample	I_c (μA)	β_L	L_{loop} (pH)	$\omega_r/2\pi$ (GHz)	E_J/h (THz)	Q_{ext}	Q_{int}
JPA 1	2.34 ± 0.01	0.087 ± 0.001	38.3 ± 0.1	5.829 ± 0.001	1.16 ± 0.01	310-380	>30000
JPA 2	2.19 ± 0.12	0.096 ± 0.008	45.4 ± 4.7	5.863 ± 0.018	1.09 ± 0.06	265-300	>30000
JPA 3	12.16 ± 0.08	0.535 ± 0.001	45.5 ± 0.3	6.214 ± 0.001	6.04 ± 0.04	5300 ± 100	1300 ± 30
JPA 4	9.82 ± 0.12	0.552 ± 0.001	58.2 ± 0.7	6.164 ± 0.001	4.88 ± 0.06	12000 ± 1000	1100 ± 100
JPA 5	9.64 ± 0.27	0.556 ± 0.001	59.6 ± 1.7	6.216 ± 0.003	4.79 ± 0.14	72000 ± 13000	1280 ± 300

For resonators, the internal and external quality factors are important quantities. The internal quality factor Q_{int} provides information about the internal losses of the resonator while the external quality factor Q_{ext} is mainly given by the coupling capacitance C_c, which determines the coupling strength of the resonator to the signal port [40]. To extract the quality factors and the resonant frequencies for different external flux values, the expression [41]

$$S_{11} = \frac{(\omega-\omega_0)^2 + i\kappa_{int}(\omega-\omega_0) + (\kappa_{ext}^2 - \kappa_{int}^2)/4}{\left[(\omega-\omega_0) + i(\kappa_{ext}+\kappa_{int})/2\right]^2}, \quad (7)$$

for the reflection coefficient, obtained from an input-output theory, is fitted to the experimental data. Here, $\kappa_{ext} = \omega_0/Q_{ext}$ and $\kappa_{int} = \omega_0/Q_{int}$ are the external and the internal loss rates, respectively. The measurements are performed in the low power regime with less than one photon on average inside the resonator. For samples JPA 1 and JPA 2, we extract internal quality factors $Q_{int} \gtrsim 3\times10^4$ depending on the external flux while the external quality factors Q_{ext} decrease with increasing JPA resonant frequency ω_0. Both samples show an overcoupled behavior. Furthermore, we observe a strongly undercoupled behavior for samples JPA 3 to JPA 5, where the external quality factor is much larger than the internal quality factor. Moreover, for these samples, Q_{ext} as well as Q_{int} are flux independent and Q_{int} is lower than the one of samples JPA 1 and JPA 2. The low Q_{int} for the sample batch containing JPA 3 to JPA 5 is explained by intensive Ar ion milling before evaporation of the Al which degrades the quality of the metal-substrate interface leading to increased losses [42]. Furthermore, for JPA 1 and JPA 2 the extracted Q_{ext} coincide well with the design target of 200 while for JPA 3 to JPA 5 the extracted Q_{ext} deviate substantially from the design target.

Figure 4 shows the flux-dependent JPA resonant frequencies for two samples together with numerical fits according to Eq. (4) where the critical current I_c, the screening parameter β_L and the bare resonator frequency $\omega_r/2\pi$ are used as fitting parameters. In the experimentally accessed frequency range, Eq. (4) holds with an error of less than 0.5% compared to the exact solution from Eq. (1). Using $L_r = 2\,\mathrm{nH}$ estimated from the geometric design parameters and the characteristic impedance of the transmission line, $Z_0 = 50\,\Omega$, one can extract several relevant JPA parameters from the data as summarized in Tab. I. In order to quantitatively model the flux dependence of JPA 1 and JPA 2, the decrease of the JPA resonant frequency with increasing absolute value of Φ_{ext} has to be taken into account. This can be achieved by considering the flux dependence of the kinetic inductance of the resonator [43], which leads to a flux dependent bare resonator frequency $\omega_r(\Phi_{ext}) = \omega_r(0)[1-\gamma\Phi_{ext}^2]$. Here, γ is a constant depending on the material and geometry of the resonator.

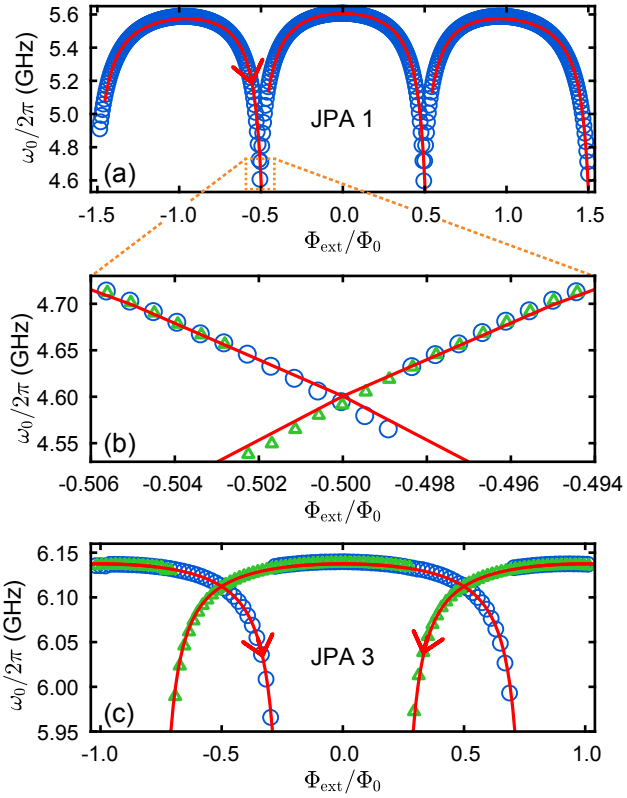

Figure 4. JPA resonant frequency ω_0 of (a,b) JPA 1 and (c) JPA 3 as a function of the applied flux Φ_{ext} as well as numerical fits (red lines). Blue circles and green triangles mark the data taken for increasing and decreasing Φ_{ext}, respectively, with arrows further indicating the sweep direction. The JPAs are stabilized at temperatures between 17 mK and 50 mK. Error bars of ω_0 from fits of Eq. (7) are smaller than the symbol size. The fit for JPA 1 in (a,b) is shown for $\gamma = 5.8 \times 10^{-3}\,\mathrm{Wb}^{-2}$. The fitting results are summarized in Tab. I.

For the two samples, JPA 1 and JPA 2, a weak hysteretic behavior is experimentally observed [see Fig. 4(a) and Fig. 4(b)]. All in all, the fit describes the experimental data very well. However, the simulations predict a more pronounced hysteresis than observed in the experimental data. We attribute the observed deviation to a finite noise floor which causes a premature hopping of the phase particle to an adjacent minimum. Therefore, it is expected that the hysteresis is not as pronounced in the experimental data as predicted by simulations.

For the three other samples, JPA 3 to JPA 5, a strong hysteretic behavior is observed in the resonant frequency versus applied flux dependence. As an example, Fig. 4(c) shows an overlay of both sweep directions of the external flux for JPA 3. The flux dependence is described very well by the model calculations. The hysteresis over a large frequency window is explained by larger screening parameters β_{L} as compared to JPA 1 and JPA 2. With increasing β_{L}, the rigid coupling between the two phase differences across the junctions is lost, allowing for multiple classes of minimal energy states of the dc-SQUID for a given external flux. These different classes of minimal energy states manifest themselves in different resonant frequencies of the JPA. For the measured samples, we find only two such classes whereas even more can exist for sufficiently large β_{L}. Depending on the history of the dc-SQUID regarding the external flux, different eligible minimal energy states are occupied by the dc-SQUID and, thus, a hysteretic behavior when changing the sweep direction of the external flux is observed.

To avoid this hysteresis, one would prefer a negligible L_{loop} by choosing small dc-SQUID loop areas. However, to allow for an efficient coupling to the pump line, the loop area for flux-pumped parametric devices is usually chosen to be on the order of $10\,\mu\mathrm{m}^2$ [3, 11, 12, 36]. From numerical estimations with FastHenry3 [44] we obtain the total loop inductance $L_{\mathrm{loop}} \simeq 30\,\mathrm{pH}$ consisting of both the geometrical inductance of the loop itself and the kinetic inductance, where the latter dominates due to the thin superconducting dc-SQUID electrodes. In order to minimize the hysteretic behavior of the JPAs while still maintaining a sufficient coupling to the pump line, one could reduce the kinetic inductance by choosing a dc-SQUID design with thicker Al electrodes in future devices. Since all JPAs have the same dc-SQUID loop design, we attribute the spread in the extracted values of L_{loop} to variations of the kinetic inductance originating from differences during the fabrication process of the JPAs. Regarding the critical currents I_{c} for the sample batch containing JPA 1 and JPA 2, the extracted values are consistent with the design value of $2\,\mu\mathrm{A}$, while they significantly exceed the design values of $4\,\mu\mathrm{A}$ for the sample batch containing JPA 3 to JPA 5. The larger values of I_{c} for this sample batch are most likely caused by an excessive outgassing process of the resist mask during the Al evaporation which causes fluctuations in the Josephson junction parameters.

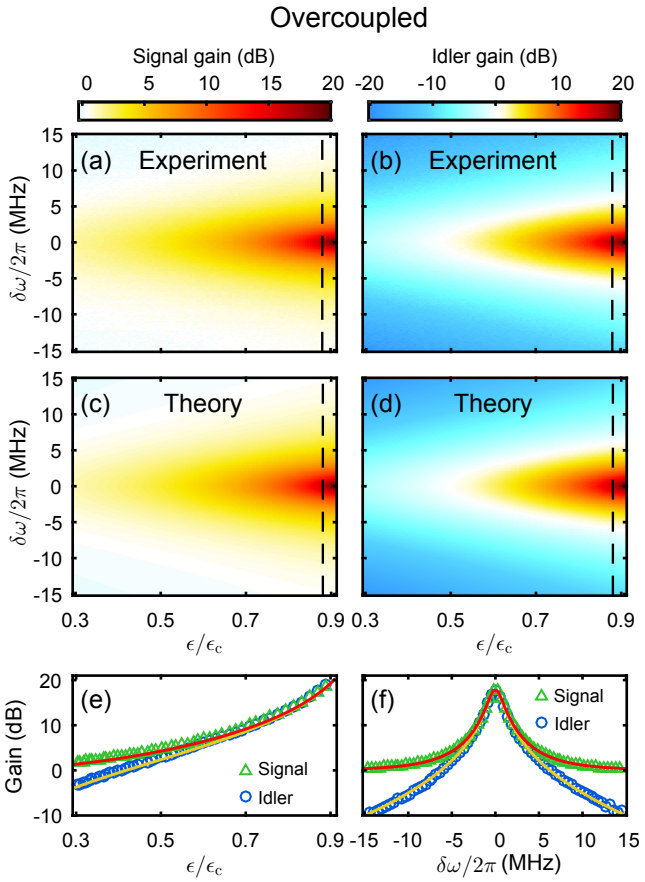

Figure 5. (a,b) Experimental spectra of the nondegenerate signal and idler gains as a function of ϵ and signal detuning $\delta\omega$ from half the pump frequency of $\omega_{\mathrm{pump}}/4\pi = 5.4\,\mathrm{GHz}$ for JPA 1. The smallest detuning is $|\delta\omega|/2\pi = 0.15\,\mathrm{MHz}$. (c,d) Theoretical calculations with $g \simeq 3.49\,\mathrm{V}^{-1}$ of the signal and idler gains computed from Eqs. (8) and (9), respectively. (e) Maximal signal and idler gains extracted from Lorentzian fits along vertical cuts in (a,b). (f) Signal and idler gains as a function of the signal frequency along the dashed lines. The symbols mark the experimental data and solid lines are fits of the data by Eqs. (8) and (9). The JPA temperature is stabilized at 50 mK.

VI. NONDEGENERATE GAIN

In this section, we investigate the nondegenerate gain of two JPAs, where one JPA has an overcoupled behavior and the other one has an undercoupled behavior. To this end, a flux value corresponding to a certain resonant frequency ω_0 of the JPA is fixed. Then, a pump tone with frequency $\omega_{\mathrm{pump}} = 2\omega_0$ is applied to the JPA. Regarding the input signal, the JPA is operated in the nondegenerate mode, meaning that the frequency of the applied signal $\omega_{\mathrm{s}} = \omega_{\mathrm{pump}}/2 + \delta\omega$ always has a non-zero offset from half the pump frequency, $\delta\omega \neq 0$. In order to evaluate the experimental data we use explicit expressions for the nondegenerate gain for the case of a flux-driven JPA. The nondegenerate signal gain $G_{\mathrm{s}}(\delta\omega)$ and idler gain $G_{\mathrm{i}}(\delta\omega)$

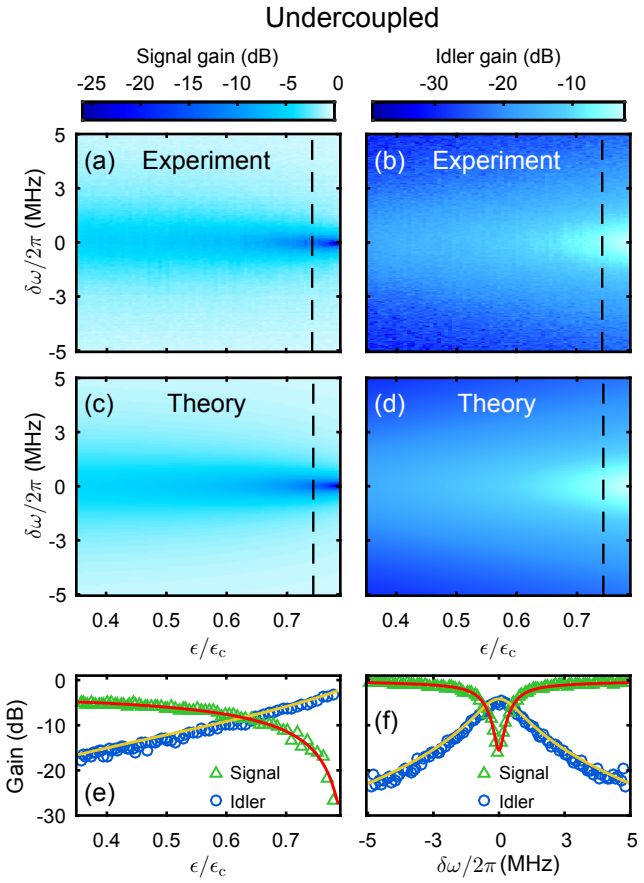

Figure 6. (a,b) Experimental spectra of the nondegenerate signal and idler gains as a function of ϵ and signal detuning $\delta\omega$ from half the pump frequency of $\omega_{\rm pump}/4\pi = 6.125\,$GHz for JPA 3. The smallest detuning is $|\delta\omega|/2\pi = 25\,$kHz. (c,d) Theoretical calculations with $g \simeq 0.17\,{\rm V}^{-1}$ of the signal and idler gains computed from Eqs. (8) and (9), respectively. (e) Maximal signal and idler gains extracted from Lorentzian fits along vertical cuts in (a,b). (f) Signal and idler gains as a function of the signal frequency along the dashed lines. The symbols mark the experimental data and solid lines are fits of the data by Eqs. (8) and (9). The JPA temperature is stabilized at 30 mK.

for $\omega_{\rm pump} = 2\omega_0$ are given by [41]

$$G_{\rm s}(\delta\omega) = \frac{\kappa_{\rm int}^2\delta\omega^2 + \left[(\kappa_{\rm int}^2 - \kappa_{\rm ext}^2)/4 - \epsilon^2\omega_0^2 - \delta\omega^2\right]^2}{\kappa_{\rm tot}^2\delta\omega^2 + \left[\kappa_{\rm tot}^2/4 - \epsilon^2\omega_0^2 - \delta\omega^2\right]^2}\,, \tag{8}$$

$$G_{\rm i}(\delta\omega) = \frac{\kappa_{\rm ext}^2\epsilon^2\omega_0^2}{\kappa_{\rm tot}^2\delta\omega^2 + \left[\kappa_{\rm tot}^2/4 - \epsilon^2\omega_0^2 - \delta\omega^2\right]^2}\,, \tag{9}$$

where $\kappa_{\rm tot}$ is the total resonator loss and $\epsilon = gA_{\rm pump}$ is related to the root-mean-squared pump amplitude $A_{\rm pump}$ at the sample box via a coupling constant g. Eqs. (8) and (9) are only valid for $\epsilon \le \epsilon_{\rm c} = \kappa_{\rm tot}/2\omega_0$.

Figure 5(a) and Figure 5(b) show the nondegenerate signal and idler gains as a function of ϵ for the overcoupled JPA 1. The pump frequency is fixed at $\omega_{\rm pump}/2\pi = 10.8\,$GHz corresponding to a flux working point of $\Phi_{\rm ext} = 0.39\,\Phi_0$ with $Q_{\rm ext} = 365$, $Q_{\rm int} \gtrsim 3\times10^4$ and $\epsilon_c = 1.39\times10^{-3}$. We measure the idler gain by comparing the generated idler mode at frequency $\omega_{\rm i} = \omega_{\rm pump}/2 - \delta\omega$ to the applied signal at frequency $\omega_{\rm s} = \omega_{\rm pump}/2 + \delta\omega$. Amplification can only be observed within a frequency window defined by the resonator bandwidth and centered at the resonant frequency. In this region, we observes an increased gain for both the signal and idler mode with increasing pump power. Theoretical predictions from Eqs. (8) and (9) are depicted in Fig. 5(c) and Fig. 5(d) for the signal and the idler mode, respectively. Only the coupling constant $g \simeq 3.49\,{\rm V}^{-1}$ is used as a fitting parameter, while the quality factors and the resonant frequency are fixed to previously determined experimental values. The given values for g include an additional uncertainty due to the fact that $A_{\rm pump}$ is calculated from the power at the output of the microwave source using an estimated pump line attenuation of 61 dB. Figure 5(e) shows the maximal signal and idler gains extracted from the detuning dependence and Fig. 5(f) shows the signal and idler spectra at a fixed ϵ. As it can be seen, the model reproduces both the signal and idler modes very well.

In addition, the undercoupled sample JPA 3 is investigated in the nondegenerate mode by applying a fixed pump tone of frequency $\omega_{\rm pump}/2\pi = 12.25\,$GHz. The flux working point is $\Phi_{\rm ext} = -0.40\,\Phi_0$ with $Q_{\rm ext} = 5283$, $Q_{\rm int} = 1267$ and $\epsilon_c = 4.89\times10^{-4}$. The experimentally obtained spectra of the signal and idler as a function of the pump power are depicted in Fig. 6(a) and Fig. 6(b). For $\delta\omega/2\pi \simeq 50\,$kHz, the incident signal is increasingly deamplified by up to $-30\,$dB with increasing pump power, while the idler gain increases. Since these undercoupled devices are described well by our parametric amplifier theory, we still call them JPAs although they do not act as amplifiers but rather as attenuators. Again Fig. 6(c) and Fig. 6(d) depict theoretical predictions with $g \simeq 0.17\,{\rm V}^{-1}$ as the only fitting parameter. They reproduce the experimentally observed behavior accurately. The deamplification behavior of JPA 3 is in strong contrast to sample JPA 1 where the signal gain increases with increasing pump power. To understand this behavior qualitatively, we simplify Eq. (8) for $\delta\omega \to 0$ and obtain

$$G_{\rm s} \approx \frac{\left[(\kappa_{\rm int}^2 - \kappa_{\rm ext}^2)/4 - \epsilon^2\omega_0^2\right]^2}{\left[\kappa_{\rm tot}^2/4 - \epsilon^2\omega_0^2\right]^2}\,. \tag{10}$$

If the sample is overcoupled ($\kappa_{\rm ext} > \kappa_{\rm int}$), the numerator of Eq. (10) is monotonously increasing while the denominator is monotonously decreasing with increasing ϵ. However, for an undercoupled JPA ($\kappa_{\rm ext} < \kappa_{\rm int}$) the numerator crosses zero for a certain threshold value $\epsilon = \epsilon_{\rm crit} < \epsilon_{\rm c}$, meaning that the signal is increasingly deamplified with increasing ϵ until the threshold is reached. In the overcoupled regime, the JPA acts as an amplifier for an incident signal, whereas for undercoupled JPAs the incident signal is deamplified depending on the pump power. In

this case, the device is no longer an amplifier but acts as a tunable microwave attenuator.

The input-output model yielding Eqs. (8) and (9) directly relates the material and design parameters such as internal and external quality factors to the amplification performance of the JPAs. For example, it predicts that increasing Q_{int} from 10^4 to 10^5, for $Q_{\mathrm{ext}} = 365$, results in a maximal gain improvement of 3 dB at a fixed pump power. Nevertheless, in the high gain limit higher order nonlinear effects, which are not included in the model, might limit the amplification of the JPAs [33].

VII. CONCLUSION

In summary, we have developed an efficient approach to describe the hysteretic dependence of the resonant frequency ω_0 of flux-driven Josephson parametric amplifiers on the applied magnetic flux. We have achieved this by classical simulations of the position of the phase particle in the flux-dependent two-dimensional potential landscape of a dc-SQUID which strongly depends on the screening parameter β_{L}. Furthermore, we have applied a distributed-element model to describe ω_0 of the JPA.

In contrast to the textbook discussion of the total flux in a dc-SQUID as a function of the external flux, where hysteretic behavior is predicted only for $\beta_{\mathrm{L}} \geqslant 2/\pi$, we obtain a hysteretic flux dependence of the resonant frequency of dc-SQUID based JPAs already for $\beta_{\mathrm{L}} \ll 2/\pi$. This prediction is convincingly corroborated by our experiments. The observed hysteretic behavior of the investigated JPAs is clearly related to different magnitudes of their screening parameters $0.09 \leqslant \beta_{\mathrm{L}} \leqslant 0.56$ arising from different critical current values of their Josephson junctions. A hysteretic flux dependence of JPAs is usually unwanted for their typical use as low noise amplifiers and therefore makes the fundamental understanding of the origin of the hysteresis an important issue for the further development and optimization of JPAs. In our particular case, we directly show that high critical currents, which are otherwise helpful for increasing the 1 dB compression point, lead to hysteresis in our flux-driven JPAs. Furthermore, our experiments show that the JPA resonant frequency can be used for a non-invasive readout of the dc-SQUID state which can be used to prepare the dc-SQUID in a specific state.

Additionally, the nondegenerate gain of JPAs with different resonator characteristics has been investigated. We have observed that, in the undercoupled regime, a JPA can act as a tunable microwave attenuator with attenuation of up to −30 dB, while an overcoupled JPA acts as a linear amplifier, as expected. The experimentally observed behavior is accurately reproduced by model calculations based on a simple, linearized and explicit formalism for the flux-driven JPA. Overall, the presented work allows for the engineering of JPA parameters, such as critical current, loop inductance, internal and external quality factors, depending on the desired application.

ACKNOWLEDGMENTS

We acknowledge support by the German Research Foundation through SFB 631 and FE 1564/1-1, the EU projects PROMISCE and SCALEQIT, the Elite Network of Bavaria through the program ExQM, the International Max Planck Research School "Quantum Science and Technology", the projects JST ERATO (Grant No. JPMJER1601) and JSPS KAKENHI (Grant No. 26220601, 15K17731) as well as the ImPACT Program of Council for Science. We would like to thank K. Kusuyama for assistance with part of the JPA fabrication.

[1] C. Macklin, K. O'Brien, D. Hover, M. E. Schwartz, V. Bolkhovsky, X. Zhang, W. D. Oliver, and I. Siddiqi, "A near-quantum-limited Josephson traveling-wave parametric amplifier," Science **350**, 307 (2015).

[2] T. C. White, J. Y. Mutus, I.-C. Hoi, R. Barends, B. Campbell, Yu Chen, Z. Chen, B. Chiaro, A. Dunsworth, E. Jeffrey, J. Kelly, A. Megrant, C. Neill, P. J. J. O'Malley, P. Roushan, D. Sank, A. Vainsencher, J. Wenner, S. Chaudhuri, J. Gao, and J. M. Martinis, "Traveling wave parametric amplifier with Josephson junctions using minimal resonator phase matching," Appl. Phys. Lett. **106**, 242601 (2015).

[3] T. Yamamoto, K. Inomata, M. Watanabe, K. Matsuba, T. Miyazaki, W. D. Oliver, Y. Nakamura, and J. S. Tsai, "Flux-driven Josephson parametric amplifier," Appl. Phys. Lett. **93**, 042510 (2008).

[4] J. Y. Mutus, T. C. White, R. Barends, Yu Chen, Z. Chen, B. Chiaro, A. Dunsworth, E. Jeffrey, J. Kelly, A. Megrant, C. Neill, P. J. J. O'Malley, P. Roushan, D. Sank, A. Vainsencher, J. Wenner, K. M. Sundqvist, A. N. Cleland, and J. M. Martinis, "Strong environmental coupling in a Josephson parametric amplifier," Appl. Phys. Lett. **104**, 263513 (2014).

[5] C. Eichler and A. Wallraff, "Controlling the dynamic range of a Josephson parametric amplifier," EPJ Quan. Tech. **1**, 2 (2014).

[6] N. Roch, E. Flurin, F. Nguyen, P. Morfin, P. Campagne-Ibarcq, M. H. Devoret, and B. Huard, "Widely tunable, nondegenerate three-wave mixing microwave device operating near the quantum limit," Phys. Rev. Lett. **108**, 147701 (2012).

[7] B. Yurke, M. L. Roukes, R. Movshovich, and A. N. Pargellis, "A low-noise series-array Josephson junction parametric amplifier," Appl. Phys. Lett. **69**, 3078 (1996).

[8] M. A. Castellanos-Beltran and K. W. Lehnert, "Widely tunable parametric amplifier based on a superconducting quantum interference device array resonator," Appl. Phys. Lett. **91**, 083509 (2007).

[9] N. Bergeal, F. Schackert, M. Metcalfe, R. Vijay, V. E. Manucharyan, L. Frunzio, D. E. Prober, R. J. Schoelkopf, S. M. Girvin, and M. H. Devoret, "Phase-preserving amplification near the quantum limit with a Josephson ring

modulator," Nature **465**, 64 (2010).
[10] M. Hatridge, R. Vijay, D. H. Slichter, J. Clarke, and I. Siddiqi, "Dispersive magnetometry with a quantum limited SQUID parametric amplifier," Phys. Rev. B **83**, 134501 (2011).
[11] L. Zhong, E. P. Menzel, R. Di Candia, P. Eder, M. Ihmig, A. Baust, M. Haeberlein, E. Hoffmann, K. Inomata, T. Yamamoto, Y. Nakamura, E. Solano, F. Deppe, A. Marx, and R. Gross, "Squeezing with a flux-driven Josephson parametric amplifier," New J. Phys. **15**, 125013 (2013).
[12] M. Simoen, C. W. S. Chang, P. Krantz, J. Bylander, W. Wustmann, V. Shumeiko, P. Delsing, and C. M. Wilson, "Characterization of a multimode coplanar waveguide parametric amplifier," J. Appl. Phys. **118**, 154501 (2015).
[13] B. Yurke, L. R. Corruccini, P. G. Kaminsky, L. W. Rupp, A. D. Smith, A. H. Silver, R. W. Simon, and E. A. Whittaker, "Observation of parametric amplification and deamplification in a Josephson parametric amplifier," Phys. Rev. A **39**, 2519 (1989).
[14] M. A. Castellanos-Beltran, K. D. Irwin, G. C. Hilton, L. R. Vale, and K. W. Lehnert, "Amplification and squeezing of quantum noise with a tunable Josephson metamaterial," Nat. Phys. **4**, 929 (2008).
[15] E. P. Menzel, F. Deppe, M. Mariantoni, M. Á. Araque Caballero, A. Baust, T. Niemczyk, E. Hoffmann, A. Marx, E. Solano, and R. Gross, "Dual-path state reconstruction scheme for propagating quantum microwaves and detector noise tomography," Phys. Rev. Lett. **105**, 100401 (2010).
[16] C. Eichler, D. Bozyigit, C. Lang, M. Baur, L. Steffen, J. M. Fink, S. Filipp, and A. Wallraff, "Observation of two-mode squeezing in the microwave frequency domain," Phys. Rev. Lett. **107**, 113601 (2011).
[17] F. Mallet, M. A. Castellanos-Beltran, H. S. Ku, S. Glancy, E. Knill, K. D. Irwin, G. C. Hilton, L. R. Vale, and K. W. Lehnert, "Quantum state tomography of an itinerant squeezed microwave field," Phys. Rev. Lett. **106**, 220502 (2011).
[18] E. A. Tholén, A. Ergül, K. Stannigel, C. Hutter, and D. B. Haviland, "Parametric amplification with weak-link nonlinearity in superconducting microresonators," Phys. Scr. **T137**, 014019 (2009).
[19] B. Yurke and E. Buks, "Performance of cavity-parametric amplifiers, employing Kerr nonlinearites, in the presence of two-photon loss," J. Lightw. Technol. **24**, 5054 (2006).
[20] E. P. Menzel, R. Di Candia, F. Deppe, P. Eder, L. Zhong, M. Ihmig, M. Haeberlein, A. Baust, E. Hoffmann, D. Ballester, K. Inomata, T. Yamamoto, Y. Nakamura, E. Solano, A. Marx, and R. Gross, "Path entanglement of continuous-variable quantum microwaves," Phys. Rev. Lett. **109**, 250502 (2012).
[21] K. G. Fedorov, L. Zhong, S. Pogorzalek, P. Eder, M. Fischer, J. Goetz, E. Xie, F. Wulschner, K. Inomata, T. Yamamoto, Y. Nakamura, R. Di Candia, U. Las Heras, M. Sanz, E. Solano, E. P. Menzel, F. Deppe, A. Marx, and R. Gross, "Displacement of propagating squeezed microwave states," Phys. Rev. Lett. **117**, 020502 (2016).
[22] E. Flurin, N. Roch, F. Mallet, M. H. Devoret, and B. Huard, "Generating entangled microwave radiation over two transmission lines," Phys. Rev. Lett. **109**, 183901 (2012).
[23] R. Di Candia, K. G. Fedorov, L. Zhong, S. Felicetti, E. P. Menzel, M. Sanz, F. Deppe, A. Marx, R. Gross, and E. Solano, "Quantum teleportation of propagating quantum microwaves," EPJ Quan. Tech. **2**, 25 (2015).
[24] S. Lloyd, "Enhanced sensitivity of photodetection via quantum illumination," Science **321**, 1463 (2008).
[25] S.-H. Tan, B. I. Erkmen, V. Giovannetti, S. Guha, S. Lloyd, L. Maccone, S. Pirandola, and J. H. Shapiro, "Quantum illumination with Gaussian states," Phys. Rev. Lett. **101**, 253601 (2008).
[26] U. L. Andersen, J. S. Neergaard-Nielsen, P. van Loock, and A. Furusawa, "Hybrid discrete- and continuous-variable quantum information," Nat. Phys. **11**, 713 (2015).
[27] C. Weedbrook, S. Pirandola, R. García-Patrón, N. J. Cerf, T. C. Ralph, J. H. Shapiro, and S. Lloyd, "Gaussian quantum information," Rev. Mod. Phys. **84**, 621 (2012).
[28] W. H. Louisell, A. Yariv, and A. E. Siegman, "Quantum fluctuations and noise in parametric processes. I," Phys. Rev. **124**, 1646 (1961).
[29] J. P. Gordon, W. H. Louisell, and L. R. Walker, "Quantum fluctuations and noise in parametric processes. II," Phys. Rev. **129**, 481 (1963).
[30] A. A. Clerk, M. H. Devoret, S. M. Girvin, F. Marquardt, and R. J. Schoelkopf, "Introduction to quantum noise, measurement, and amplification," Rev. Mod. Phys. **82**, 1155 (2010).
[31] G. J. Dolan, "Offset masks for lift-off photoprocessing," Appl. Phys. Lett. **31**, 337 (1977).
[32] M. Wallquist, V. S. Shumeiko, and G. Wendin, "Selective coupling of superconducting charge qubits mediated by a tunable stripline cavity," Phys. Rev. B **74**, 224506 (2006).
[33] W. Wustmann and V. Shumeiko, "Parametric resonance in tunable superconducting cavities," Phys. Rev. B **87**, 184501 (2013).
[34] P. Bhupathi, P. Groszkowski, M. P. DeFeo, M. Ware, F. K. Wilhelm, and B. L. T. Plourde, "Transient dynamics of a superconducting nonlinear oscillator," Phys. Rev. Appl. **5**, 024002 (2016).
[35] M. Tinkham, *Introduction to Superconductivity*, 2nd ed. (McGraw-Hill, New York, 1996).
[36] M. Sandberg, C. M. Wilson, F. Persson, T. Bauch, G. Johansson, V. Shumeiko, T. Duty, and P. Delsing, "Tuning the field in a microwave resonator faster than the photon lifetime," Appl. Phys. Lett. **92**, 203501 (2008).
[37] V. Lefevre-Seguin, E. Turlot, C. Urbina, D. Esteve, and M. H. Devoret, "Thermal activation of a hysteretic dc superconducting quantum interference device from its different zero-voltage states," Phys. Rev. B **46**, 5507 (1992).
[38] F. Balestro, J. Claudon, J. P. Pekola, and O. Buisson, "Evidence of two-dimensional macroscopic quantum tunneling of a current-biased dc SQUID," Phys. Rev. Lett. **91**, 158301 (2003).
[39] E. Hoskinson, F. Lecocq, N. Didier, A. Fay, F. W. J. Hekking, W. Guichard, O. Buisson, R. Dolata, B. Mackrodt, and A. B. Zorin, "Quantum dynamics in a camel-back potential of a dc SQUID," Phys. Rev. Lett. **102**, 097004 (2009).
[40] J. Goetz, F. Deppe, M. Haeberlein, F. Wulschner, C. W. Zollitsch, S. Meier, M. Fischer, P. Eder, E. Xie, K. G. Fedorov, E. P. Menzel, A. Marx, and R. Gross, "Loss mechanisms in superconducting thin film microwave resonators," J. Appl. Phys. **119**, 015304 (2016).

[41] T. Yamamoto, K. Koshino, and Y. Nakamura, *Principles and Methods of Quantum Information Technologies*, edited by Y. Yamamoto and K. Semba, Vol. 911 (Springer Japan, 2016) pp. 495–513.

[42] C. M. Quintana, A. Megrant, Z. Chen, A. Dunsworth, B. Chiaro, R. Barends, B. Campbell, Yu Chen, I.-C. Hoi, E. Jeffrey, J. Kelly, J. Y. Mutus, P. J J O'Malley, C. Neill, P. Roushan, D. Sank, A. Vainsencher, J. Wenner, T. C. White, A. N. Cleland, and John M. Martinis, "Characterization and reduction of microfabrication-induced decoherence in superconducting quantum circuits," Appl. Phys. Lett. **105**, 062601 (2014).

[43] J. E. Healey, T. Lindström, M. S. Colclough, C. M. Muirhead, and A. Ya Tzalenchuk, "Magnetic field tuning of coplanar waveguide resonators," Appl. Phys. Lett. **93**, 043513 (2008).

[44] Mattan Kamon, M.J. Ttsuk, and J.K. White, "FASTHENRY: a multipole-accelerated 3-D inductance extraction program," IEEE Trans. Microw. Theory Tech. **42**, 1750 (1994).